Research in Astronomy and Astrophysics, 24:065013 (14pp), 2024 June https://doi.org/10.1088/1674-4527/ad420e

Probing the Gamma-Ray Emission Region of Five TeV Flat Spectrum Radio Quasars

Hu-Bing Xiao[1], Hai-Tao Cao[2], Rui Xue[3], Jin-Ting Cai[4], Ge-Ge Wang[5], Marina Manganaro[6], Shao-Hua Zhang[1], Zhi-Hao Ouyang[1], Li-Ping Fu[1], and Jun-Hui Fan[7,8,9]

[1] Shanghai Key Lab for Astrophysics, Shanghai Normal University, Shanghai 200234, China
[2] School of Information Engineering, Guangzhou Panyu Polytechnic, Guangzhou 511483, China
[3] Department of Physics, Zhejiang Normal University, Jinhua 321004, China; ruixue@zjnu.edu.cn
[4] College of Mathematics and Physics, Guangxi Minzu University, Nanning 530006, China
[5] Key Laboratory of Cosmology and Astrophysics (Liaoning), College of Sciences, Northeastern University, Shenyang 110819, China
[6] Department of Physics, University of Rijeka, Rijeka 51000, Croatia
[7] Center for Astrophysics, Guangzhou University, Guangzhou 510006, China
[8] Key Laboratory for Astronomical Observation and Technology of Guangzhou, Guangzhou 510006, China
[9] Astronomy Science and Technology Research Laboratory of Department of Education of Guangdong Province, Guangzhou 510006, China
Received 2023 December 25; revised 2024 April 3; accepted 2024 April 22; published 2024 May 28

Abstract

The location of γ-ray emission of blazars remains a contested topic, inspiring the development of numerous investigative techniques to address this issue. In this work, we analyzed Fermi γ-ray light curves in the GeV and MeV bands, employing the discrete cross-correlation function method to discern time lags between the two bands. For 4C +21.35, Ton 599, B2 1420+32, and PKS 1510-089, we identified a time lag spanning several days, while for PKS 1441+25, the time lag was not statistically found. The results imply that the soft photons necessary for inverse Compton scattering predominantly originate from the dusty torus in the first four sources, whereas for PKS 1441+25, they seem to be sourced mainly from the broad-line region. Further analysis of the opacity ($\tau_{\gamma\gamma}$) and the GeV spectra study supports the conclusion that the location of the dissipation region must be beyond the BLR to avoid significant absorption. Notably, for PKS 1441+25, the emission region is also posited to lie outside yet proximate to the BLR. The parameters of describing the emission region were obtained by fitting broadband spectral energy distribution with contemporaneous observation data. Our findings suggest that for the five TeV FSRQs, during TeV flaring events, the jet appears to maintain an equilibrium between the energy density of the magnetic field and that of the particles for all investigated sources, with the exceptions of 4C +21.35 and PKS 1441+25. In terms of the overall jet power, particle energy is the dominant contributor, and the observed blazar radiation cannot be solely attributed to the magnetic field, except in the case of 4C +21.35. Consequently, magnetic reconnection is unlikely to be the primary mechanism behind particle acceleration in these systems.

Key words: galaxies: active – gamma-rays: galaxies – galaxies: jets

1. Introduction

Blazars, as the most extreme subclass of active galactic nuclei (AGNs), are known to host a relativistic jet oriented toward the observers. The jet orientation preference raises various extreme observational properties, such as rapid and large amplitude variability, high and variable polarization, strong and variable γ-ray emissions, and apparent superluminal motion (Wills et al. 1992; Urry & Padovani 1995; Fan 2002; Villata et al. 2006; Fan et al. 2014; Xiao et al. 2015; Gupta et al. 2016; Xiao et al. 2019; Abdollahi et al. 2020; Fan et al. 2021; Xiao et al. 2022). There are two subclasses of blazars, namely flat spectrum radio quasars (FSRQs) and BL Lacertae objects, the former is characterized by strong emission lines, while the latter shows a featureless optical spectrum or weak emission lines (Urry & Padovani 1995; Scarpa & Falomo 1997). A typical blazar broadband spectral energy distribution (SED) forms a two-hump structure. The lower energy bump is attributed to the synchrotron radiation of the relativistic electrons. However, the origin of the higher energy bump remains controversial. In the leptonic scenario, the higher energy bump is attributed to the inverse Compton (IC) scattering, which can be further divided into synchrotron-self Compton (SSC) if the soft photons come from the synchrotron process, or external Compton (EC) if the soft photons come from external photon field, e.g., the accretion disk (Dermer & Schlickeiser 1993), the broad-line region (BLR) (Sikora et al. 1994; Fan et al. 2006), and the dusty torus (DT) (Błażejowski et al. 2000; Arbeiter et al. 2002; Sokolov & Marscher 2005). The hadronic model could also explain the higher-energy bump through proton synchrotron radiation and secondary particle cascade (Mücke & Protheroe 2001; Dimitrakoudis et al. 2012; Zheng & Kang 2013; Diltz et al. 2015), and the hadronic model

seems promising since the detection of the neutrino event that is associated with blazar (TXS 0506+056) flare activity (IceCube Collaboration et al. 2018; Xue et al. 2019, 2021).

TeV emission, namely the very-high-energy (VHE) band (> 100 GeV), has been detected for a fraction of blazars Wierzcholska & Wagner (2016). The first TeV emission of a blazar was reported by the Whipple telescope in 1992, and this event was confirmed to be associated with the famous blazar Mrk 421 (Punch et al. 1992). Later observation established more blazars with TeV emission, e.g., Mrk 501, 1ES 2344 +514, and PKS 2155-304 (Quinn et al. 1996; Catanese et al. 1998; Chadwick et al. 1999), thus the extragalactic background light (EBL) absorption must have been overestimated and the TeV detection mainly dependent on the redshift and the sensitivity of the telescopes. Ground-based Cherenkov observatories, including Major Atmospheric Gamma Imaging Cherenkov telescopes (MAGIC), the High Energy Stereoscopic System telescopes (H.E.S.S), the Very Energetic Radiation Imaging Telescope Array System (VERITAS) and the Large High Altitude Air Shower Observatory (LHAASO), among others, are dedicated to exploring the VHE γ-ray sky of the Universe. Currently, about one-third of the TeV sources (intragalactic and extragalactic) are confirmed as blazars, suggesting that blazars make a significant contribution to TeV emission background, and TeV emission should relate to extreme activities in the Universe. At the time of writing, the mechanism behind blazar TeV emission remains poorly understood.

One of the key problems of the TeV emission study is determining the location of the emission region. The observation of VHE photons supports the theory of emission occurring outside the BLR and within the DT (Donea & Protheroe 2003; Liu & Bai 2006), because VHE photons would be severely attenuated by the photons in BLR due to the $\gamma + \gamma \rightarrow e^{\pm}$ interaction. However, the observed hour-scale TeV variability for blazars (Aleksić et al. 2011; H.E.S.S. Collaboration et al. 2021) yields a very compact emission region. If the conventional assumption is employed, wherein the full jet cross-section is considered to be the same size as the diameter of the emission region, this would imply that the emission region is located inside the BLR. Additional methods are required to resolve this contradiction.

The EC process is widely accepted for the high energy emission of FSRQs, with the seed photons mainly coming from the BLR for the emission region located inside the BLR, and from the DT for the emission region located outside the BLR. One of the key differences between BLR and DT seed photons is that the seed photons of the BLR have higher energies than those of the DT. This difference results in different electron cooling timescales, with cooling timescales being shorter at higher energies. Consequently, emission from the DT would exhibit a time lag of hours between the cooling of the MeV and GeV components of a flare (Foschini et al. 2011). Brown (2013) analyzed time lags for the blazar PKS 1510-089, based on 3.5 yr of observations from the Fermi Large Area Telescope (Fermi-LAT), and found evidence for the presence of multiple γ-ray emission regions located in both the BLR and DT region. Similarly, Acharyya et al. (2021) analyzed γ-ray flux for nine FSRQs and found evidence supporting both BLR and DT origins.

For the purpose of investigating the location and the properties of the TeV γ-ray emission region, in this work, we analyzed Fermi γ-ray light curves and calculated contemporaneous SEDs in the frame of leptonic models. In Section 2, we define our source selection; Fermi γ-ray data analysis and light curve analysis will be described in Section 3; The broadband SED modeling is presented in Section 4; The discussion will be provided in Section 5; Section 6 presents the main conclusions.

2. Sample and Data Acquisition

The main goal of this work is to locate and study the emission region responsible for the TeV emission of FSRQs. There are nine FSRQs that have been reported as TeV emitters and introduced in TeVCat 2.0.[10] We managed to collect both published Fermi γ-ray observation data and contemporaneous multi-wavelength observation data during the TeV emission campaign for five of the nine FSRQs.

2.1. 4C +21.35

4C +21.35, also known as PKS 1222+216, is an FSRQ with a redshift $z = 0.432$. MAGIC detected a TeV emission in a short observation period (~0.5 hr) on 2010 June 17 (Mariotti 2010), in which the flux varies significantly within the 30 minute exposure, implying a flux doubling time of about 10 minutes (8.6 minutes, Aleksić et al. 2011). The spectrum extends from about 70 GeV up to at least 400 GeV and was well described by a power-law function with a photon index $\Gamma = 3.75$. The averaged integral flux above 100 GeV was $4.6 \times 10^{-10}\,\mathrm{cm^{-2}\,s^{-1}}$ (~1 Crab) (Aleksić et al. 2011). At the same time, the Astro rivelatore Gamma a Immagini Leggero and Fermi-LAT detected a massive flare activity coinciding with the VHE event (Iafrate et al. 2010; Striani et al. 2010), and the multi-wavelength SED modeling of this event had been performed by, e.g., Tavecchio et al. (2011). VERITAS observed a TeV γ-ray excess between 2014 February 26 and March 10 (MJD 56714-56726), starting 11 days after a bright GeV flare reported by the Fermi-LAT Collaboration. The integral flux above 100 GeV corresponds to $(1.4 \pm 0.3) \times 10^{-11}\,\mathrm{ph\,cm^{-2}\,s^{-1}}$ (~3% Crab) (Holder 2014), and Fermi-LAT detected a coincident flare with fast decay timescale of 10.4 ± 6.2 days (Adams et al. 2022). Adams et al. (2022) performed a contemporaneous multi-wavelength (Steward, Swift, Fermi-LAT, VERITAS) study during the corresponding VHE emission (2014 February 26–March 10 for 4C +21.35) period. We collect the multi-wavelength data from

[10] http://tevcat2.uchicago.edu/

Adams et al. (2022) and use them for the 4C +21.35 SED modeling study in this work.

2.2. Ton 599

Ton 599 is an FSRQ located at redshift 0.7247 (Hewett & Wild 2010) and is one of the highest redshift objects detected in the VHE energy range. It was found as a TeV blazar by MAGIC and VERITAS on the nights of 2017 December 15 and 16 (MJD 58102-58103; Mirzoyan 2017; Mukherjee & VERITAS Collaboration 2017) after it was reported in a GeV high state in 2017 October (Cheung et al. 2017). VERITAS detected the corresponding average flux observed in the two nights above 100 GeV to be about $(1.0 \pm 0.1) \times 10^{-10}\,\mathrm{cm}^{-2}\,\mathrm{s}^{-1}$ (~16% Crab), and Fermi-LAT detected a coincident flare with fast decay timescale of 11.8 ± 1.1 days (Adams et al. 2022). A contemporaneous multi-wavelength observation study from 2017 December 15 to 16 was performed in Adams et al. (2022), in which they analyzed optical *V* and *R* band data from the Steward observatory public archive,[11] ultraviolet (UV)/optical (170–550 nm) and X-ray (0.2–10 keV) data from Neil Gehrels Swift Observatory, the Fermi-LAT Pass 8 data for the GeV band spectrum, and the VERITAS TeV data during corresponding VHE emission period (2017 December 15–16). We collect the multi-wavelength data from Adams et al. (2022) and use them for the Ton 599 SEDs modeling study in this work.

2.3. B2 1420+32

B2 1420+32, with a redshift $z = 0.682$, was classified as an FSRQ based on its radio spectral property (Healey et al. 2007). At the beginning of 2020, it underwent an enhanced flux state and was observed by ground- and space-based instruments. The entire observation was divided into four episodes denoting pre-flare, optical flare, VHE flare and post-flare. MAGIC detected the VHE flare during 2020 January 20–22 (MJD = 58868.3-58870.3), the flux reached $7.8 \times 10^{-11}\,\mathrm{cm}^{2}\,\mathrm{s}^{-1}$ and the unattenuated spectrum was well fitted by a power-law function with a spectral index 4.04 (MAGIC Collaboration et al. 2021). A doubling time was not obtained with MAGIC due to a limited observation time caused by the bad weather; however, a strong flare with a variability timescale of a few days was observed in the optical band during the VHE flare (MAGIC Collaboration et al. 2021). MAGIC Collaboration et al. (2021) performed a multi-wavelength study of this source and modeled four states of SEDs employing the 15 GHz radio data from Owens Valley Radio Observatory, the near-infrared data acquired with the camera CANICA (Carrasco et al. 2017) and the Observatorio Astrofísico Guillermo Haro 2.1 m telescope, the optical data from several ground-based telescopes, X-ray data from Swift and XMM-Newton space telescopes, the GeV data from Fermi-LAT and TeV data from MAGIC. The VHE flare is of interest to our work, and we collect the multi-wavelength contemporaneous data from MAGIC Collaboration et al. (2021) and use them for the B2 1420+32 SED modeling study.

2.4. PKS 1441+25

PKS 1441+25, with a redshift $z = 0.939$, is one of the most distant TeV FSRQs. Both VERITAS and MAGIC collaborations announced the VHE γ-ray detection in 2015 April (Mirzoyan 2015a; Mukherjee 2015). Extensive multi-wavelength observation was performed contemporaneously by many telescopes including VERITAS, MAGIC, Fermi-LAT, Swift, etc. in the period of 2015 April 18–28 (MJD 57130–MJD 57140). Ahnen et al. (2015) conducted a multi-wavelength study and suggested a subdivision of the high state into two distinct flux states. Moreover, they claimed a variability timescale of 6.4 ± 1.9 days in the band covered by MAGIC. Abeysekara et al. (2015) stated that no variability was established during this period of the VHE detection based on the VERITAS data. The TeV emission average flux was above 80 GeV was $5.0 \times 10^{-11}\,\mathrm{cm}^{2}\,\mathrm{s}^{-1}$ and an intrinsic photon index was 3.4 after EBL correction (Abeysekara et al. 2015; Sahakyan & Gasparyan 2017). We collect PKS 1441+25 multi-wavelength contemporaneous data from Abeysekara et al. (2015), where they obtained optical *V*-band data from All-Sky Automated Survey for Supernovae optical data, optical/UV and X-ray data from Swift and NuSTAR, GeV band data from Fermi-LAT, and the TeV band data from VERITAS to form the broadband SED.

2.5. PKS 1510-089

PKS 1510-089 is a bright FSRQ located at redshift $z = 0.36$. It was not established to exhibit VHE γ-ray radiation until 2009 March–April when H.E.S.S. claimed the detection of VHE integral flux of $1 \times 10^{-11}\,\mathrm{cm}^{-2}\,\mathrm{s}^{-1}$ (H. E. S. S. Collaboration et al. 2013). A high state was observed in 2015 May by Fermi-LAT, which was also evident in the optical and infrared (IR) bands. Moreover, MAGIC and H.E.S.S both detected TeV emissions from this source (Mirzoyan 2015b; Jankowsky et al. 2015; Sameer et al. 2015; Ahnen et al. 2017; Zacharias et al. 2017). Two periods, period A (MJD 57160-57161) and period B (MJD 57164-57166), of TeV emission were observed by MAGIC during 2015 May. The EBL correction was performed for both periods of spectra, with intrinsic spectral indexes of 3.17 and 4.33 for period A and period B, respectively (Ahnen et al. 2017). The doubling time of the PKS 1510-089 flare was found as 1 hr at GeV band (Saito et al. 2013) and further reported as 1.3 hr (Prince et al. 2017). The multi-wavelength contemporaneous data, including the 37 GHz radio data from Metsähovi observations, the IR to UV data from ground-based telescopes, the X-ray data from Swift, GeV γ-ray data from Fermi-LAT, and TeV data from MAGIC for both periods A and B, from Ahnen et al. (2017) will be used in this work.

[11] http://james.as.arizona.edu/~psmith/Fermi/

3. Fermi-LAT γ-Ray Data Analysis

3.1. The γ-Ray Light Curves

Fermi-LAT monitors the γ-ray sky every three hours in the energy range from 20 MeV to above 300 GeV (Atwood et al. 2009). We analyzed the publicly available Pass 8 database for the region of interest (ROI) of a 10° radius centered at the positions of our sources, and photon events with zenith angles less than 90° were selected to reduce the contamination from the Earth's limb. We used the LAT science tool Fermitools 2.2.0, instrument response function P8R3_SOURCE_V3, and Galactic and isotropic diffuse emission functions gll_iem_v07 and iso_P8R3_SOURCE_V3_v1 respectively. These light curves were constructed in 3 hr bins through a standard binned maximum likelihood analysis and are shown in Figure 1. Data points are retained only if the maximum likelihood Test Statistic (TS) values are larger than 9.

In this work, we only employ two-month episodes of Fermi data to do analyses for each source; the episode starts one month before the VHE detection date and ends one month after the VHE detection, as shown in Table 1. On one hand, the episode ensures the simultaneity between Fermi MeV-GeV band emission and the emission of the VHE band. On the other hand, a short episode should be able to keep the light curve difference, which will be introduced in the next section, between the MeV (100 MeV–1 GeV) and the GeV (1–300 GeV) band from dilution of the long-term episode (e.g., 15 yr).

3.2. Light Curve Correlation Analysis

Blazar emission in the high energy ranges, within the framework of a leptonic model, is attributed to the IC scattering. The scattering can occur in either the Thomson regime ($\gamma\epsilon_0 \ll 1$) or in the Klein-Nishina (KN) regime ($\gamma\epsilon_0 \gg 1$), in which γ is the electron energy in units of Lorentz factor and ϵ_0 denotes the incident photon energy in units of electron rest energy. Dotson et al. (2012) found that the scattering occurs in the Thomson regime when incident photons come from the DT (IR photons) and in the KN regime when incident photons come from the BLR (UV photons). In the former case, the relativistic electron energy dissipation rate $\dot{\gamma} \propto \gamma^2$, leading to an electron cooling time $t_c = \gamma/\dot{\gamma} \propto 1/\gamma$ that makes the cooling timescale energy-dependent. In the latter case, the relativistic electron energy dissipation rate $\dot{\gamma} \propto \ln\gamma$, resulting in an electron cooling time $t_c = \gamma/\dot{\gamma} \propto \gamma/\ln\gamma$ that makes the cooling timescale energy-independent. Considering an electron population with a certain spectrum (e.g., power-law, log-parabola, etc) scattering monochrome soft photons, higher energy electrons scatter the incident soft photon to higher energies when the cross-section is constant. Consequently, the cooling timescale should be significantly shorter for higher energy electrons than for the lower energy electrons in the case of scattering in the Thomson regime. Thus, one could expect, in the case of soft photons coming from the DT, a time lag between the cooling that produces the MeV and GeV emission (Dotson et al. 2012; Acharyya et al. 2021).

To investigate the time lag between the MeV and GeV light curves, we conduct the cross-correlation of light curves between these two bands. The fundamental concept in analyzing the correlation between two data series involves calculating their correlation coefficient. In the discrete correlation function (DCF), considering two data sets, the unbinned correlation is expressed as

$$\mathrm{UDCF_{ij}} = \frac{(a_i - \bar{a}) \times (b_j - \bar{b})}{\sqrt{\sigma_a^2 - \sigma_b^2}}, \quad (1)$$

where a_i and b_i refer to the time series, $\bar{a}$ and $\bar{b}$ are the mean values, and the σ_a and σ_b are the corresponding standard deviations of the two data sets. The $\mathrm{UDCF_{ij}}$ with the same delay is then averaged to obtain the DCF in a suitable size bin for each time interval, expressed as

$$\mathrm{DCF} = \frac{1}{M}\sum \mathrm{UDCF_{ij}}, \quad (2)$$

where M represents the number of data pairs (Edelson & Krolik 1988; Hufnagel & Bregman 1992). However, the time lag may be diluted by a long time interval, as one band's emission could precede the emission from the other during a specific period, but they could travel synchronously for the rest of the time. To mitigate lag dilution, we only utilize two months of data that cover the TeV emission campaign for time lag analysis.

We calculate the DCF of the light curves using the PyDCF[12] method (Robertson et al. 2015). Cross-correlation plots for pairs of GeV and MeV band light curves, for a lag of ±60 days, are depicted in Figure 2. A bootstrap method is then applied to obtain the confidence limits of the correlation (e.g., Ezhikode et al. 2022) between MeV and GeV band light curves. This involves simulating 50,000 random subsets of the original light-curve pairs, with each subset containing 80% of the original data points. The PyDCF method is then applied to these simulated pairs over a lag range of ±60 days with a flexible lag bin width, ranging from 1 to 15, to determine the most promising DCF distribution. The centroid DCF of the cross-correlation functions is determined from the DCF values and the confidence intervals (68.27%, 95.45%, and 99.73%) of the peak DCF are obtained with the simulations, as shown in the upper panel of Figure 2 and Table 2. In order to assess the significance of correlations, we estimate the 1σ, 2σ, and 3σ confidence levels for the distributions of simulated DCF after subtracting the original DCF value for each lag, displayed in the lower panel of Figure 2. Our results indicate that the observed correlation is significant at the 3σ level for 4C

[12] https://github.com/astronomerdamo/pydcf

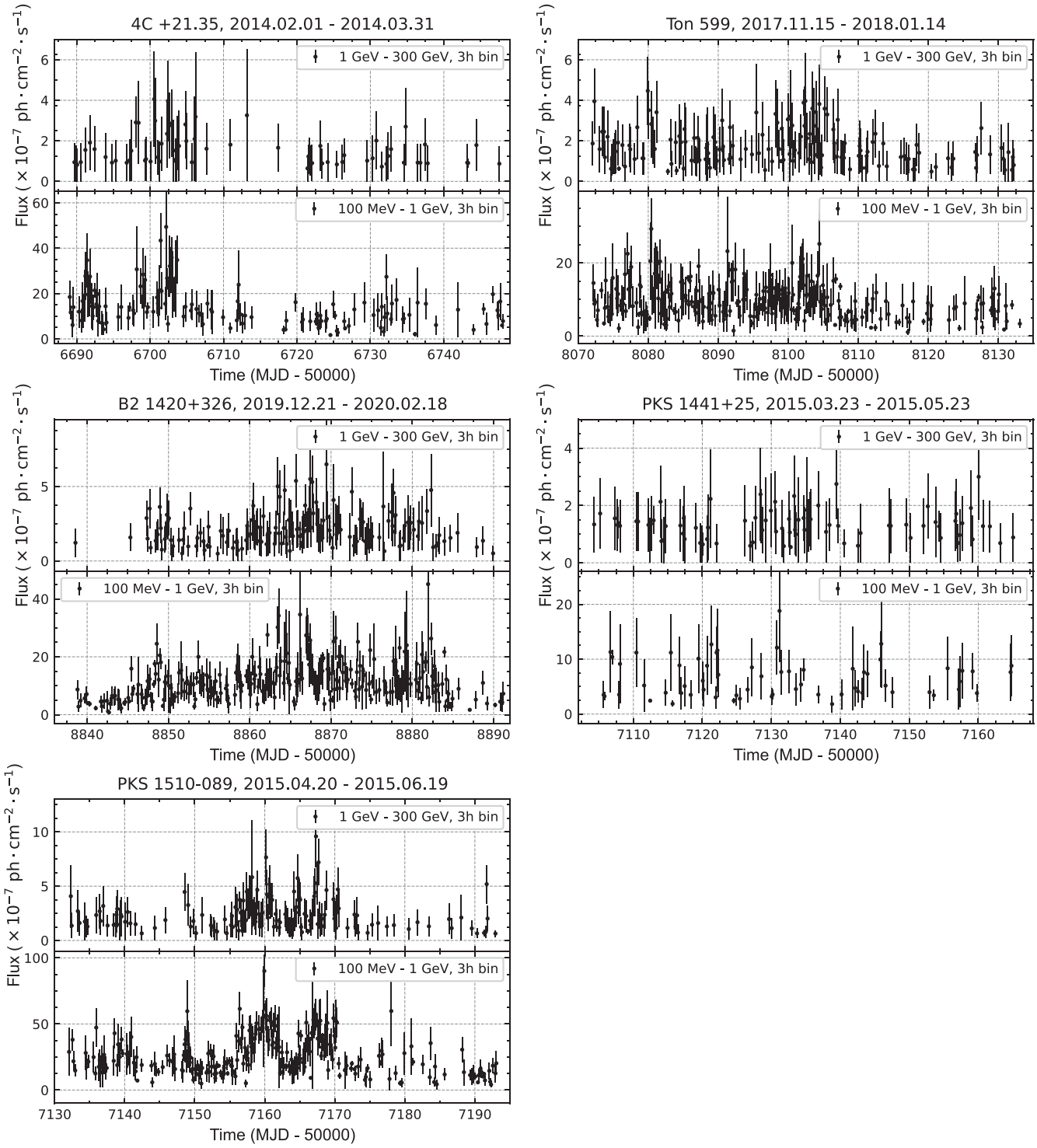

Figure 1. The Fermi γ-ray light curves for the five sources. The light curves are presented in the GeV band (1–300 GeV, the upper panel) and the MeV band (100 MeV–1 GeV, the lower panel). The light curves span two months and the data points are presented in 3 hr bin.

Table 1
The Fermi γ-Ray Light Curve Information

Name (1)	VHE Observation Date (2)	VHE Detection (3)	Fermi Light Curve Episode (4)
4C +21.35	Feb 26–Mar 10, 2014 (MJD 56714-56726)	VERITAS	2014-02-01 00:00:00, 2014-03-31 00:00:00
Ton 599	Dec 15-16, 2017 (MJD 58102-58103)	VERITAS	2017-11-15 00:00:00, 2018-01-14 00:00:00
B2 1420+32	Jan 20–22, 2020 (MJD 58868-58 870)	MAGIC	2019-12-21 00:00:00, 2020-02-18 00:00:00
PKS 1441+25	Apr 21–28, 2015 (MJD 57133-57140)	VERITAS	2015-03-23 00:00:00, 2015-05-23 00:00:00
PKS 1510-089(A)	May 18–19, 2015 (MJD 57160-57161)	MAGIC	2015-04-20 00:00:00, 2015-06-19 00:00:00
PKS 1510-089(B)	May 22–24, 2015 (MJD 57164-57166)	MAGIC	2015-04-20 00:00:00, 2015-06-19 00:00:00

+21.35, Ton 599, B2 1420+326, and PKS 1510-089, but no significant DCF was confirmed for PKS 1441+25.

4. Physical Properties of the Emission Region

4.1. The Optical Depth of $\gamma\gamma$ Pair Production

In the AGN environment, the most commonly considered external photon fields are the BLR and the DT. Following Hayashida et al. (2012), we can estimate the energy densities of the BLR and the DT in the AGN frame as

$$u_{\rm BLR}^{\rm AGN}(r^{\rm AGN}) = \frac{\eta_{\rm BLR} L_{\rm disk}}{4\pi r_{\rm BLR}^{\rm AGN\,2} c[1 + (r^{\rm AGN}/r_{\rm BLR}^{\rm AGN})^3]}, \quad (3)$$

and

$$u_{\rm DT}^{\rm AGN}(r^{\rm AGN}) = \frac{\eta_{\rm DT} L_{\rm disk}}{4\pi r_{\rm DT}^{\rm AGN2} c[1 + (r^{\rm AGN}/r_{\rm DT}^{\rm AGN})^4]}, \quad (4)$$

where $\eta_{\rm BLR} = \eta_{\rm DT} = 0.1$ are the fractions of the disk luminosity $L_{\rm disk}$ reprocessed into BLR and DT radiation, respectively, and $r^{\rm AGN}$ is the distance between the position of the emission region and the supermassive black hole (SMBH). The radiation from both BLR and DT is taken as an isotropic graybody with a peak at $\nu_{\rm BLR}^{\rm AGN} = 2 \times 10^{15}$ Hz (Tavecchio & Ghisellini 2008) and $\nu_{\rm DT}^{\rm AGN} = 3 \times 10^{13}$ Hz (Cleary et al. 2007) in the AGN frame, respectively. As suggested by the reverberation mapping, the characteristic distance of BLR is $r_{\rm BLR}^{\rm AGN} = 0.1 (L_{\rm disk}/10^{46}\ {\rm erg\ s^{-1}})^{1/2}$ pc and the characteristic distance of DT is $r_{\rm DT}^{\rm AGN}=2.5(L_{\rm disk}/10^{46}\,{\rm erg\,s^{-1}})^{1/2}$ pc (Suganuma et al. 2006; Kishimoto et al. 2011; Bentz et al. 2013; Pozo Nuñez et al. 2014). Thus, Equations (3) and (4) become

$$u_{\rm BLR}^{\rm AGN}(r^{\rm AGN}) = 2.8 \times 10^{-2}\,{\rm erg\,cm^{-3}} \frac{1}{1 + ({\rm r}^{\rm AGN}/{\rm r}_{\rm BLR}^{\rm AGN})^3}, \quad (5)$$

and

$$u_{\rm DT}^{\rm AGN}(r^{\rm AGN}) = 4.5 \times 10^{-5}\,{\rm erg\,cm^{-3}} \frac{1}{1 + ({\rm r}^{\rm AGN}/{\rm r}_{\rm DT}^{\rm AGN})^4}. \quad (6)$$

By integrating from the position of emission region to infinity (Xue et al. 2022), we calculate the integrated $\gamma\gamma$ opacity $\tau_{\gamma\gamma}(r^{\rm AGN})$ for the highest energy photons of each FSRQ, as depicted in Figure 3. It can be seen that the emission region has to be located outside the BLR to prevent the highest energy photons from being absorbed.

It is well known that photons above $\sim 1/16 (m_{\rm e}c^2)^2/(h\nu_{\rm BLR}^{\rm AGN}) \approx 2.6$ GeV are emitted in the KN regime if soft photons are dominated by the BLR, and photons above $\sim 1/16 (m_{\rm e}c^2)^2/(h\nu_{\rm DT}^{\rm AGN}) \approx 175$ GeV are emitted in the KN regime if soft photons are dominated by the DT. Since 0.1–1 GeV flare is found to be delayed compared to the 1–300 GeV flare in previous studies, external photons should mainly come from the DT. This result is consistent with those obtained by the analysis of $\gamma\gamma$ opacity shown in Figure 3. On the other hand, if the BLR is the dominant external photon field, a hundred GeV flare should be delayed compared to the 0.1–1 GeV flare because of the KN effect.

4.2. The Broadband Spectral Energy Distribution

In the aforementioned discussion, the study of $\gamma\gamma$ opacity suggests the emission region has to be located outside the BLR for TeV emission to avoid attenuation from BLR soft photons. Moreover, time lags we derived in the previous section also suggest a DT origin of soft photons for Ton 599, B2 1420 +326, 4C +21.35 and PKS 1510-089, but the result of time lag could not sufficiently constrain the emission region location for PKS 1441+25.

The measurement of time lags between variations in different energy bands provides an important restriction on the physical parameters in the framework of the one-zone model. A natural way to explain these lags is to interpret them as due to the cooling time of relativistic electrons (e.g., Takahashi et al. 1996). Since 0.1–1 GeV and 1–300 GeV emissions are both from the EC_DT (DT is the dominant photon field) scattering, the observed time lag $\Delta T^{\rm obs}$ can be estimated as

$$\Delta T^{\rm obs} = \frac{3 m_{\rm e} c}{4\sigma_{\rm T} u_{\rm DT}^{\rm AGN} \Gamma^2 \delta}\left(\frac{1}{\gamma_{0.1-1\ {\rm GeV}}} - \frac{1}{\gamma_{1-300\ {\rm GeV}}}\right), \quad (7)$$

where $\sigma_{\rm T}$ is the Thomson scattering cross section, and γ is the electron Lorentz factor. Here we set $\Gamma = \delta$ for FSRQs. Using

Figure 2. The cross-correlation between GeV γ-ray and MeV γ-ray band light curves of the five sources. The upper panel of each subfigure shows the distribution of the centroid lag values obtained from cross-correlation analysis. The solid pink vertical line indicates the peak of the distribution ($\tau_{\rm peak}$). The confidence limits of $\tau_{\rm peak}$ are plotted in red, green, and blue dashed lines. The lower panel of each subfigure displays the significance of the correlations at the 1σ (red dashed line), 2σ (green dashed line), and 3σ (blue dashed line) levels for different lags.

Table 2
The Fermi γ-Ray Light Curve Time Lag

Name (1)	$\Delta T^{\rm obs}$ (day) (2)
4C +21.35	3.11
Ton 599	1.14
B2 1420+32	1.69
PKS 1441+25	non
PKS 1510-089	1.92

the monochromatic approximation, γ can be deduced as

$$\gamma \approx \left(\frac{\nu^{\rm obs}}{\nu_{\rm DT}^{\rm AGN}}\right)^{1/2}\frac{1}{\delta}, \tag{8}$$

where $\nu^{\rm obs}$ represents the frequency in 0.1–1 GeV or 1–300 GeV. In the estimation, we take the mean values of these two ranges for simplicity. Substituting Equation (8) into Equation (7), δ can be derived

$$\delta \approx 10.6\left(\frac{1\ {\rm day}}{\Delta T^{\rm obs}}\right)^{1/2}\left(\frac{4.5\times10^{-5}\ {\rm erg\ cm^{-3}}}{u_{\rm DT}^{\rm AGN}}\right)^{1/2}. \tag{9}$$

If we assume that the dissipation occurs within the DT, the minimum values of δ for 4C 21.35, Ton 599, B2 1420+32, and PKS 1510-089 can be obtained, which are 6.0, 9.9, 8.2, and 7.7, respectively. Applying Equation (9), the energy density of the DT in the jet frame can be obtained

$$\begin{aligned} u_{\rm DT} &= u_{\rm DT}^{\rm AGN}\delta^2 \\ &= 5.1\times10^{-3}\ {\rm erg\ cm^{-3}}\left(\frac{1\ {\rm day}}{\Delta {\rm T}^{\ {\rm obs}}}\right). \end{aligned} \tag{10}$$

It can be seen that $u_{\rm DT}$ becomes a constant when the time lag is determined. Given the simultaneous SEDs of 4C +21.35, Ton 599, B2 1420+22, and PKS 1510-089 (A) and (B) are provided, we can estimate the rough ratio of $L_{\rm EC}/L_{\rm SSC}/L_{\rm syn}$, where the subscripts denote the dominant EC, SSC, and synchrotron components of GeV, X-ray, and low-energy emissions, respectively. Therefore, we have

$$L_{\rm EC}/L_{\rm SSC}/L_{\rm syn} \approx u_{\rm DT}/u_{\rm syn}/u_{\rm B}, \tag{11}$$

where $u_{\rm syn} = L_{\rm syn}/(4\pi R_{\rm diss}^2 c\delta^4)$ represents the energy density of synchrotron photons in the jet frame, and $u_{\rm B} = B^2/8/\pi$ is the energy density of the magnetic field. As suggested by Equation (10), $u_{\rm DT}$ is a constant, then values of the magnetic field B, δ, and r can be derived when the emission region size ($R_{\rm diss}$) is determined. In this work, $R_{\rm diss}$ is constrained by the observed variation timescale for four sources (4C +21.35, Ton 599, B2 1420+32, and PKS 1441+25) as $R_{\rm diss} \leqslant c\delta t_{\rm var}^{\rm obs}/(1+z)$. We utilized the Fermi-LAT flare decay timescales from Adams et al. (2022) for 4C +21.35 and for Ton 599 to constrain $R_{\rm diss}$; an optical flare with variability on the order of a few days was observed during the VHE detection of B2 1420+32 (MAGIC Collaboration et al. 2021), providing a reference to determine $R_{\rm diss}$; a VHE variability was detected by MAGIC (Ahnen et al. 2015) and the timescale was employed to determine $R_{\rm diss}$ for PKS 1441+25. For PKS 1510-089, we made adjustments with reference to the value $R_{\rm diss} = 2.8\times10^{16}$ cm from Ahnen et al. (2017), in which the $R_{\rm diss}$ was derived by giving r and jet semi-aperture angle. With these decoupled physical parameters, simultaneous SEDs can be reproduced using the conventional one-zone model. A detailed numerical model description can be found in our previous work (Xue et al. 2022). To better fit the multi-wavelength data, relativistic electrons are assumed to be injected with a broken power-law energy distribution at a constant rate. When the injection of electrons is balanced with radiative cooling and/or particle escape, a steady-state electron energy distribution (EED) is achieved. Then we apply the public *naima*[13] Python package to calculate the spectrum of the jet's non-thermal emission and to correct the GeV–TeV spectrum absorbed by the EBL (Zabalza 2015). In addition, by setting the disk luminosity $L_{\rm disk}$ and mass of SMBH $M_{\rm BH}$ in unit of $M_\odot$, the thermal emission from the accretion disk is generated via the standard disk model in Shakura & Sunyaev (1973), which assumes that the accretion disk is geometrically thin and optically thick. Modeling results are shown in Figure 4 and the derived parameters are given in Table 3.

For PKS 1441+25, we did not find clear evidence of a time lag between the MeV and the GeV emission. It might be explained if the EC_BLR process dominates the EC cooling, the process could happen either the emission region located inside the BLR or outside but very close to it. In this scenario, the electrons producing MeV emission would be in the Thomson regime, while those producing GeV emission would be in the KN regime. This makes it challenging to measure a reliable time lag between the two populations of electrons, as their cooling timescales could be similar to each other. The corresponding various cooling timescales in the observer's frame under the adopted parameter set are shown in Table 3 and in the lower panel of Figure 5. In this scenario, their theoretical time lag between two energy bands is approximately ~3 hr, which aligns closely with the 3 hr bin used in our light curve analysis. This offers a plausible explanation for why we failed to find a time lag for PKS 1441+25. A broadband SED fitting was employed to PKS 1441+25 and the fitting result is shown in the upper panel of Figure 5.

5. Discussion

5.1. The Location of the Emission Region

Determining the location of the emission region in blazars is a challenging yet crucial aspect of understanding their dynamics, particularly in relation to the soft photon

[13] https://naima.readthedocs.io/en/latest/

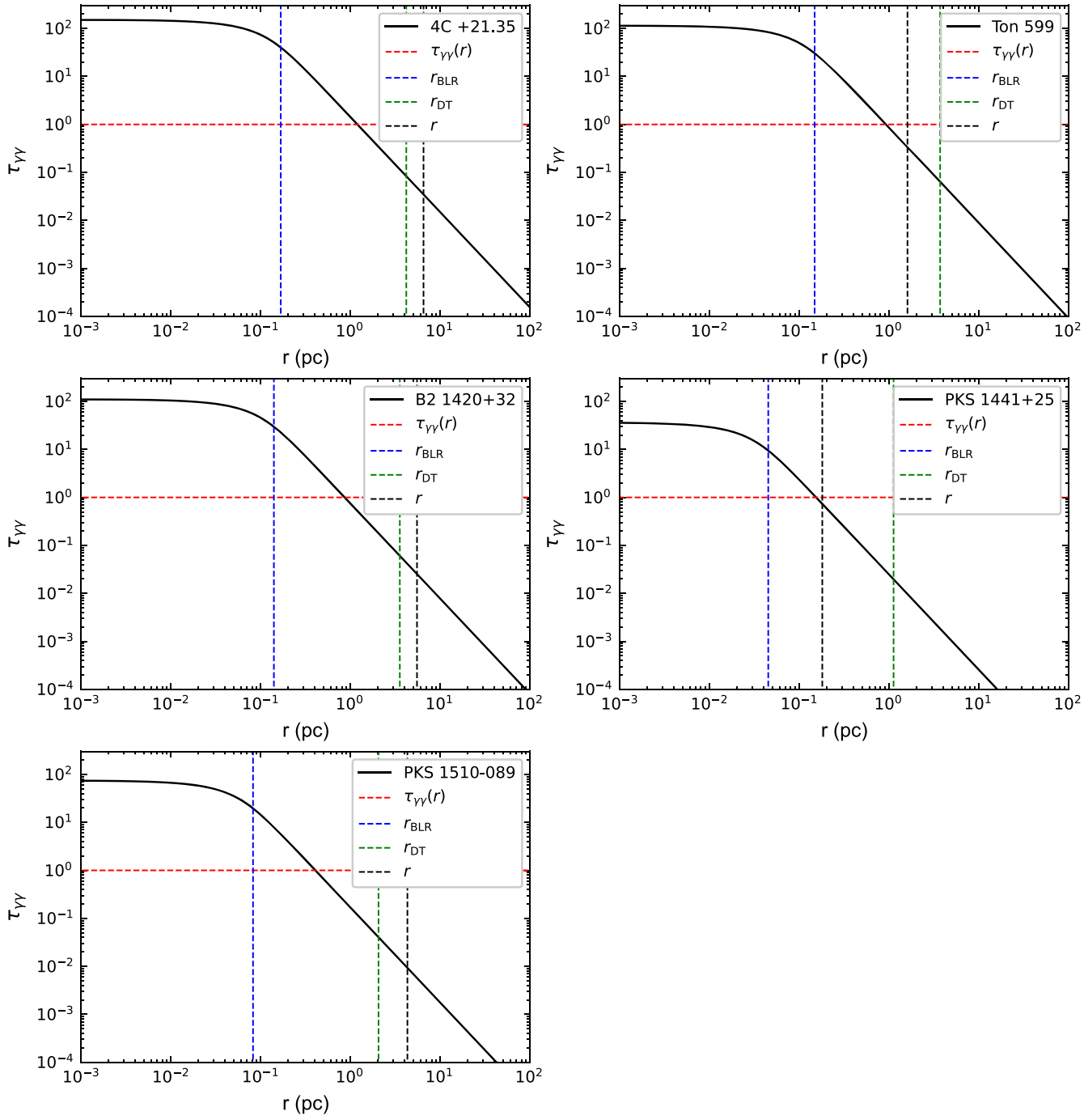

Figure 3. The $\gamma\gamma$ opacity $\tau_{\gamma\gamma}$ contributed by the BLR and DT. The opacity is a function of distance (r) from the SMBH. The black solid curves represent the opacity for the detected highest energy photons of each source. The dashed red lines stand for the $\tau_{\gamma\gamma} = 1$, and the dot–dashed blue and dashed-green vertical lines show the characteristic radii of the BLR and DT in the AGN frame, respectively.

environment. In our study, we focused on five FSRQs during their TeV detection period, employing a combination of Fermi light curve correlation analysis and the opacity of $\gamma\gamma$ pair production. The results revealed that the GeV photons preceded the MeV photons by a timescale of days (as summarized in Table 2), indicating a likely origin of scattered soft photons from the DT for all sources except PKS 1441+25. Additionally, our opacity study (detailed in 4.1) underscored the necessity of placing the emission region outside the BLR. This conclusion was drawn from the observation that $\tau_{\gamma\gamma} < 1$,

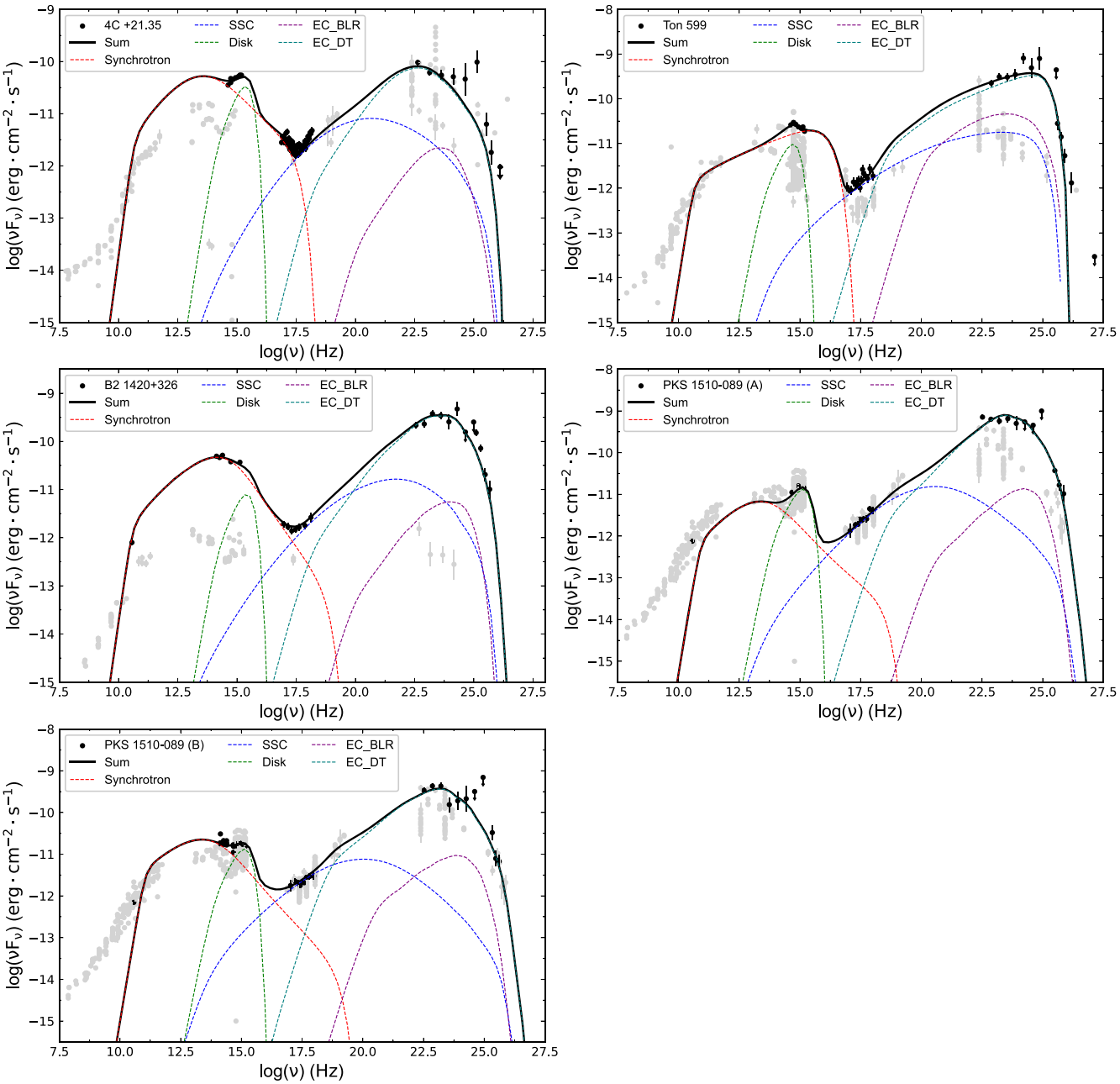

Figure 4. The fitting results of the SEDs of FSRQs with the conventional one-zone EC model. The black dots represent the multi-wavelength contemporaneously observed data, and the light-gray dots stand for the historical data from SSDC. The solid black curve represents the sum of the emission from all components, the dashed red line stands for the synchrotron emission, the dashed green line represents the emission from the accretion disk, the dashed blue line signifies the emission through the SSC process, the dashed purple line corresponds to the emission through the EC process with soft photons come from the BLR, and the dashed teal line stands for the emission through the EC process with soft photons come from the DT.

indicating minimal absorption, which aligns with the observed TeV emission.

Furthermore, the spectral GeV spectral study could also offer valuable insights into the location of the emission region. The BLR, rich in optical/UV photons, serves as a significant source of soft photons that interact with γ-ray photons, inducing characteristic breaks in the spectrum. For instance, interactions with the Lyman recombination continuum and Lyα emission of ionized helium, characterized by sufficient opacity, lead to spectral breaks at several GeVs and 10 s of GeV, respectively (Poutanen & Stern 2010). Poutanen & Stern (2010) identified such breaks at a few GeV for RGB J0920+446, PKS 045-234,

Table 3
The SED Physical Parameters

Name	B	$R_{\rm diss}$	δ	$L_{\rm inj}$	$\gamma_{\rm min}$	$\gamma_{\rm b}$	$\gamma_{\rm max}$	s_1	s_2	$L_{\rm disk}$	$M_{\rm BH}$	r	$t_{\rm var}^{\rm obs}$
	(Gs)	(cm)		(erg s^{-1})						(erg s^{-1})	($M_\odot$)	(pc)	(day)
(1)	(2)	(3)	(4)	(5)	(6)	(7)	(8)	(9)	(10)	(11)	(12)	(13)	(14)
4C +21.35	0.14	4.04E+17	15	3.0E+43	1.5E+01	3.0E+03	2.0E+05	1.5	3.2	2.8E+46[a]	1.0E+09	6.5	10.4[a]
Ton 599	0.08	3.97E+17	13	4.5E+44	2.0E+01	8.0E+04	9.0E+04	1.75	3.5	2.2E+46[a]	2.0E+09	1.6	11.8[a]
B2 1420+32	0.08	4.14E+17	20	7.0E+43	1.0E+01	1.0E+04	1.0E+06	1.5	4.0	2.0E+46[b]	1.0E+09	5.5	8.0
PKS 1510-089(A)	0.02	2.86E+16	35	2.0E+43	1.0E+01	4.1E+03	1.0E+06	1.8	4.0	6.7E+45[c]	1.0E+09	4.3	0.31
PKS 1510-089(B)	0.06	6.0E+16	35	1.0E+43	1.0E+01	3.0E+03	1.0E+06	2.0	4.0	6.7E+45[c]	1.0E+09	4.3	0.66
PKS 1441+25	0.16	2.49E+17	15	1.2E+44	1.0E+01	5.5E+03	1.0E+06	1.2	3.3	2.0E+45[d]	1.0E+09	0.18	6.4[e]

Notes.
[a] Adams et al. (2022);
[b] MAGIC Collaboration et al. (2021);
[c] Ahnen et al. (2017);
[d] Abeysekara et al. (2015);
[e] Ahnen et al. (2015). Four sources (4C +21.35, Ton599, B2 1420+32, and PKS 1510-089) are fitted with only the EC_DT model, one source (PKS 1441+25) is fitted with combined EC_BLR and EC_DT model.

PKS 1502+106 and 3C 454.3, and the significance of this evidence was then strengthened by Stern & Poutanen (2014) for 3C 454.3, suggesting an emission region located inside the BLR. Contrastingly, Costamante et al. (2018) explored spectral breaks around 10 s of GeV for 106 Fermi blazars but found no compelling evidence attributed to BLR absorption. This absence of breaks suggested an emission region situated outside the BLR. We studied the GeV spectra for the five sources in this work and drew them in Figure 6. Notably, these spectra conform well to power-law or log-parabola functions, without discernible spectral breaks in the GeV band. The consistency between our spectral analysis results, time lag study, and opacity analysis underscores that the emission region for these five sources is situated outside the BLR during the TeV-emitting period.

5.2. The SED Modeling and the Jet Power of TeV FSRQs

There are differences between SED modeling presented in this work and previous studies. For both 4C +21.35 and Ton 599, previous SED analyses, such as Adams et al. (2022), relied on EC model, presuming the emission region to be within the BLR, with soft photons originating from it. However, our investigation, incorporating time lag and opacity calculations, indicates that the dissipation region must be situated outside the BLR, with soft photons originating from the DT. Regarding B2 1420 +32, a significant difference in SED modeling lies in the magnetic field strength B. While MAGIC Collaboration et al. (2021) employed $B = 0.83$, we utilized $B = 0.08$, attributed to varying approaches in estimating the emission region size $R_{\rm diss}$. Meanwhile, the degeneration between B and δ could affect the value of B (Zhang et al. 2013). Despite both studies yielding acceptable sizes based on marginal variability timescales, MAGIC Collaboration et al. (2021) considered a timescale of 0.5–1 day, while ours employed 8 days. In the case of PKS 1510 +089, our approach diverges by employing a broken power-law

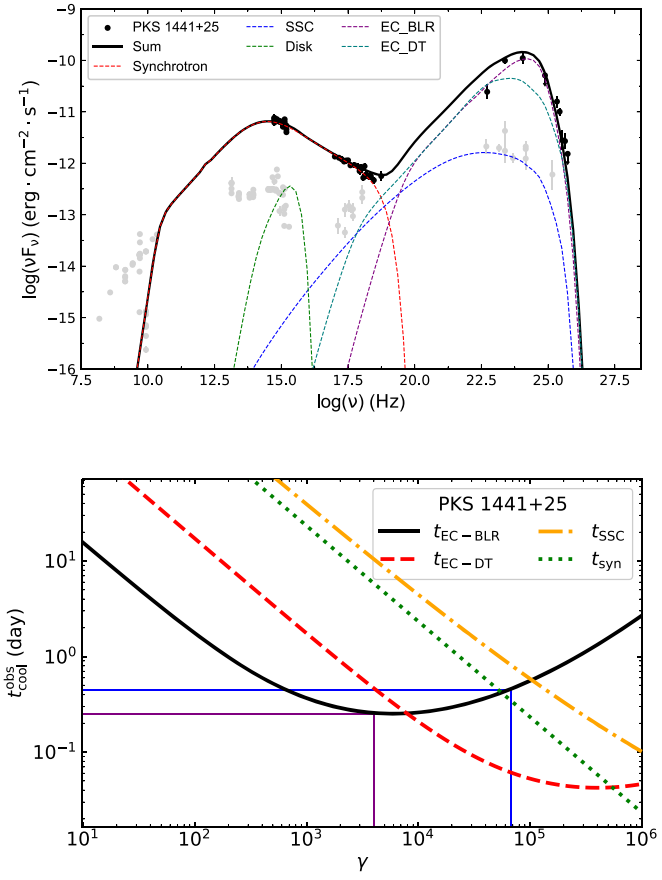

Figure 5. The SED fitting result of PKS 1441+25 with the conventional one-zone EC model (the upper panel) and the corresponding cooling timescales (the lower panel). The meaning of all curves in the upper panel has been explained in Figure 4. In the lower panel, the solid black line stands for the cooling timescale of electrons with Lorentz factor γ through EC_BLR, the dashed red line represents the cooling timescale through EC_DT, the dotted green line signifies the cooling timescale through synchrotron radiation, and the dash–dotted yellow line corresponds to the cooling timescale through SSC process. The solid purple line represents the cooling timescale for electrons scattering BLR photons to 500 MeV, and the solid blue line signifies the cooling timescale for electrons scattering BLR photons to 150 GeV.

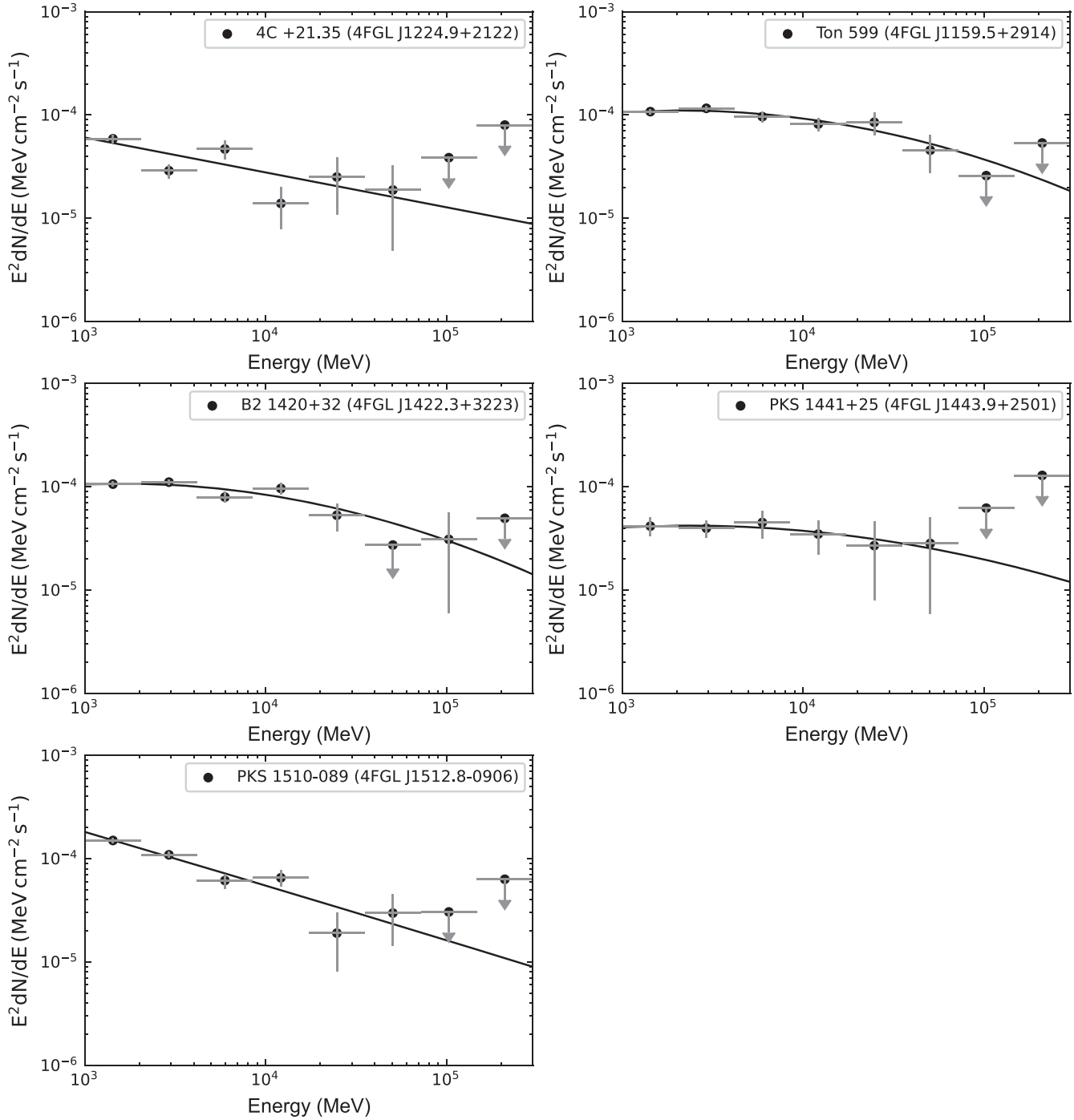

Figure 6. The Fermi γ-ray GeV (1–300 GeV) spectra for the five sources. The black dots are the GeV spectral data obtained from the same episode of the corresponding light curves, and the downward arrows represent 95% confidence level upper limits. The spectra of 4C+21.35 and PKS 1510-089 are fitted with the power law function, and the spectra of Ton 599, B2 1420+32 and PKS 1441+25 are fitted with the log-parabola function.

for the EED, as opposed to the three power-law EED utilized in Ahnen et al. (2017). Due to the different EED model, we have smaller B (0.02 for period A and 0.06 for period B) than that in their work (0.23 for period A and 0.34 for period B). PKS 1441 +25 was studied in Abeysekara et al. (2015) and its broadband SED was performed through an EC model with soft photons coming from the DT. Our study incorporates soft photons from both the BLR and the DT, with the EC_BLR peak intensity surpassing that of EC_DT, reflecting the emission region's proximity to the BLR.

Table 4
The Power of Jet and its Carriers

Name	P_e (erg s^{-1})	P_p (erg s^{-1})	P_B (erg s^{-1})	P_r (erg s^{-1})	P_{jet} (erg s^{-1})	U_e/U_B	σ_B
(1)	(2)	(3)	(4)	(5)	(6)	(7)	(8)
4C +21.35	2.15E+45	3.04E+46	2.70E+45	7.13E+44	3.60E+46	0.80	0.08
Ton 599	7.77E+45	1.71E+47	6.39E+44	9.52E+45	1.89E+47	12.22	0.004
B2 1420+32	5.53E+45	8.93E+46	1.65E+45	3.02E+45	9.95E+46	3.35	0.02
PKS 1441+25	7.85E+44	1.34E+46	1.32E+45	3.67E+45	1.92E+46	0.87	0.09
PKS 1510-089 (A)	1.55E+46	3.32E+47	1.50E+42	3.74E+44	3.48E+47	1.03×10^4	4.3×10^{-6}
PKS 1510-089 (B)	7.72E+45	2.76E+47	5.95E+43	2.05E+44	2.84E+47	129.75	2.1×10^{-4}

The determination of the jet power P_{jet} plays a crucial role in understanding the composition of blazar jets. We compute the contributions to the jet power from relativistic electrons (P_e), magnetic field (or Poynting flux, P_{mag}), radiation (P_{rad}) and cold proton kinetic (P_p) (Celotti & Ghisellini 2008; Ghisellini & Tavecchio 2010; Ding et al. 2019; Tan et al. 2020) as

$$P_{jet} = \Sigma_i \pi R_{diss}^2 \Gamma^2 c U_i, \quad (12)$$

where U_i represents the energy density of the magnetic field ($i = B$), the relativistic electron ($i = e$), cold proton ($i = p$), and bolometric radiation ($i = r$) in the comoving frame. These energy densities can be estimated as:

$$U_e = m_e c^2 \int N(\gamma)\gamma d\gamma, \quad (13)$$

$$U_p = m_p c^2 \int N(\gamma) d\gamma, \quad (14)$$

$$U_B = B^2/8\pi, \quad (15)$$

$$U_r = L_{obs}/(4\pi R_{diss}^2 c\delta^2), \quad (16)$$

where L_{obs} is the observed nonthermal bolometric jet luminosity, estimated from the SED model. The calculated values of P_e, P_p, P_B, P_r and P_{jet} are tabulated in Table 4.

In general, our analysis reveals that during the TeV emission phase, the jet power (P_{jet}) is primarily dominated by the relativistic particles. Specifically, for the sources in our sample, the electron power (P_e) surpasses the magnetic power (P_B) for Ton 599, B2 1420+32, and PKS 1510-089, with U_e/U_B ratios ranging from 3.35 to 1.03×10^4. For 4C +21.35 and PKS 1441 +25, we find that P_e is comparable to P_B, with U_e/U_B ratios of 0.80 and 0.87, respectively. This implies that the jet maintains equipartition between the magnetic field energy density and the particle energy density. Furthermore, the radiation power (P_r) exceeds the magnetic power (P_B) for all sources except 4C +21.35, indicating that the Poynting flux alone cannot account for the observed radiation.

It is found that the magnetization ratio $\sigma_B = P_B/(P_e + P_p)$ is small for all sources in our sample, suggesting that the magnetic reconnection process should not be sufficiently responsible for the particle acceleration in these sources.

6. Conclusions

In summary, our study aimed to locate and characterize the emission region of TeV FSRQs. To achieve this, we analyzed Fermi γ-ray light curves for five FSRQs, leveraging contemporaneous multi-wavelength data available during periods of TeV emission. We employed the standard Fermi data analysis process to reduce the light curve and selected data points with TS values larger than nine. Subsequent DCF analysis revealed time lags for the MeV band light curves compared to the GeV band light curves. Specifically, we found time lags of 3.11 days for 4C +21.35, 1.14 days for Ton 599, 1.69 days for B2 1420+326, and 1.92 days for PKS 1510-089. These results suggest an origin of the soft photons for IC scattering from the DT. However, for PKS 1441+25, we did not obtain clear constraints on the emission region location.

In the framework of the one-zone leptonic model, we performed the broadband SED study and investigated the physical properties of the emission region of the selected FSRQs. The broadband SEDs of 4C +21.35, Ton 599, B2 1420+326, and PKS 1510-089 are successfully fitted with EC_DT model, and the SED of PKS 1441+25 is fitted with combined EC_BLR and EC_DT model. Our SED results revealed that the jet's energy distribution is not in equipartition between magnetic field energy density and particle energy density during the TeV emission, except for 4C +21.35 and PKS 1441+25. Particularly, particle energy predominates the total jet power, suggesting that the observed blazar radiation cannot be solely attributed to magnetic field energy, except for 4C +21.35. Moreover, our study of the ratio U_e/U_B provided insights into the acceleration mechanisms of particle energy in blazar jets during TeV emission periods. The results suggest that magnetic reconnection processes cannot be the primary mechanism driving particle energy acceleration in the jets of these five sources during TeV emission events.

Acknowledgments

We thank the support from our laboratory, the Key Laboratory for Astrophysics of Shanghai, and we thank J.Biteau, A.Brill, M. Cerruti, F.D'Ammando, J.Sitarek, and M.Manganaro for their help in sharing the contemporaneous observed multi-wavelength

data. H.B.X acknowledges support from the National Natural Science Foundation of China (NSFC, Grant No. 12203034), from the Shanghai Science and Technology Fund under grant No. 22YF1431500, and from the science research grants from the China Manned Space Project. R.X acknowledges the support from the National Natural Science Foundation of China (NSFC, grant No. 12203043). L.P.F acknowledges the support from the National Natural Science Foundation of China (NSFC, grant No. 11933002). S.H.Z acknowledges support from the National Natural Science Foundation of China (NSFC, grant No. 12173026), the National Key Research and Development Program of China (grant No. 2022YFC2807303), the Shanghai Science and Technology Fund (grant No. 23010503900), the Program for Professor of Special Appointment (Eastern Scholar) at Shanghai Institutions of Higher Learning, and the Shuguang Program (23SG39) of the Shanghai Education Development Foundation and Shanghai Municipal Education Commission. J. H.F acknowledges the support from the National Natural Science Foundation of China (NSFC, grant No. U2031201, and 11733001), the Scientific and Technological Cooperation Projects (20202023) between the People's Republic of China and the Republic of Bulgaria, the science research grants from the China Manned Space Project with No. CMS-CSST-2021-A06, the support for Astrophysics Key Subjects of Guangdong Province and Guangzhou City, and this research was partially supported by the Bulgarian National Science Fund of the Ministry of Education and Science under grants KP-06- H38/4 (2019), KP-06-KITAJ/2 (2020), and KP-06-H68/4 (2022).

References

Abdollahi, S., Acero, F., Ackermann, M., et al. 2020, ApJS, 247, 33
Abeysekara, A. U., Archambault, S., Archer, A., et al. 2015, ApJL, 815, L22
Acharyya, A., Chadwick, P. M., & Brown, A. M. 2021, MNRAS, 500, 5297
Adams, C. B., Batshoun, J., Benbow, W., et al. 2022, ApJ, 924, 95
Ahnen, M. L., Ansoldi, S., Antonelli, L. A., et al. 2015, ApJL, 815, L23
Ahnen, M. L., Ansoldi, S., Antonelli, L. A., et al. 2017, A&A, 603, A29
Aleksić, J., Antonelli, L. A., Antoranz, P., et al. 2011, ApJL, 730, L8
Arbeiter, C., Pohl, M., & Schlickeiser, R. 2002, A&A, 386, 415
Atwood, W. B., Abdo, A. A., Ackermann, M., et al. 2009, ApJ, 697, 1071
Bentz, M. C., Denney, K. D., Grier, C. J., et al. 2013, ApJ, 767, 149
Błażejowski, M., Sikora, M., Moderski, R., & Madejski, G. M. 2000, ApJ, 545, 107
Brown, A. M. 2013, MNRAS, 431, 824
Carrasco, L., Hernández Utrera, O., Vázquez, S., et al. 2017, RMxAA, 53, 497
Catanese, M., Akerlof, C. W., Badran, H. M., et al. 1998, ApJ, 501, 616
Celotti, A., & Ghisellini, G. 2008, MNRAS, 385, 283
Chadwick, P. M., Lyons, K., McComb, T. J. L., et al. 1999, ApJ, 513, 161
Cheung, C. C., Gasparrini, D., & Buson, S. 2017, ATel, 10931, 1
Cleary, K., Lawrence, C. R., Marshall, J. A., Hao, L., & Meier, D. 2007, ApJ, 660, 117
Costamante, L., Cutini, S., Tosti, G., Antolini, E., & Tramacere, A. 2018, MNRAS, 477, 4749
Dermer, C. D., & Schlickeiser, R. 1993, ApJ, 416, 458
Diltz, C., Böttcher, M., & Fossati, G. 2015, ApJ, 802, 133
Dimitrakoudis, S., Mastichiadis, A., Protheroe, R. J., & Reimer, A. 2012, A&A, 546, A120
Ding, N., Gu, Q. S., Geng, X. F., et al. 2019, ApJ, 881, 125
Donea, A. C., & Protheroe, R. J. 2003, PThPS, 151, 186
Dotson, A., Georganopoulos, M., Kazanas, D., & Perlman, E. S. 2012, ApJL, 758, L15
Edelson, R. A., & Krolik, J. H. 1988, ApJ, 333, 646
Ezhikode, S. H., Shukla, A., Dewangan, G. C., et al. 2022, ApJ, 939, 76
Fan, J.-H. 2002, PASJ, 54, L55
Fan, J.-H., Bastieri, D., Yang, J.-H., et al. 2014, RAA, 14, 1135
Fan, J. H., Kurtanidze, S. O., Liu, Y., et al. 2021, ApJS, 253, 10
Fan, Z., Cao, X., & Gu, M. 2006, ApJ, 646, 8
Foschini, L., Ghisellini, G., Tavecchio, F., Bonnoli, G., & Stamerra, A. 2011, A&A, 530, A77
Ghisellini, G., & Tavecchio, F. 2010, MNRAS, 409, L79
Gupta, A. C., Agarwal, A., Bhagwan, J., et al. 2016, MNRAS, 458, 1127
Hayashida, M., Madejski, G. M., Nalewajko, K., et al. 2012, ApJ, 754, 114
Healey, S. E., Romani, R. W., Taylor, G. B., et al. 2007, ApJS, 171, 61
H.E.S.S. Collaboration, Abdalla, H., Adam, R., et al. 2021, A&A, 648, A23
H. E. S. S. Collaboration, Abramowski, A., Acero, F., et al. 2013, A&A, 554, A107
Hewett, P. C., & Wild, V. 2010, MNRAS, 405, 2302
Holder, J. 2014, ATel, 5981, 1
Hufnagel, B. R., & Bregman, J. N. 1992, ApJ, 386, 473
Iafrate, G., Longo, F., & D'Ammando, F. 2010, ATel, 2687, 1
IceCube Collaboration, Aartsen, M. G., Ackermann, M., et al. 2018, Science, 378, eaat1378
Jankowsky, F., Zacharias, M., Wierzcholska, A., et al. 2015, ATel, 7799, 1
Kishimoto, M., Hönig, S. F., Antonucci, R., et al. 2011, A&A, 536, A78
Liu, H. T., & Bai, J. M. 2006, ApJ, 653, 1089
MAGIC Collaboration, Acciari, V. A., Ansoldi, S., et al. 2021, A&A, 647, A163
Mariotti, M. 2010, ATel, 2684, 1
Mirzoyan, R. 2015a, ATel, 7416, 1
Mirzoyan, R. 2015b, ATel, 7542, 1
Mirzoyan, R. 2017, ATel, 11061, 1
Mücke, A., & Protheroe, R. J. 2001, APh, 15, 121
Mukherjee, R. 2015, ATel, 7433, 1
Mukherjee, R. & VERITAS Collaboration. 2017, ATel, 11075, 1
Poutanen, J., & Stern, B. 2010, ApJL, 717, L118
Pozo Nuñez, F., Haas, M., Chini, R., et al. 2014, A&A, 561, L8
Prince, R., Majumdar, P., & Gupta, N. 2017, ApJ, 844, 62
Punch, M., Akerlof, C. W., Cawley, M. F., et al. 1992, Natur, 358, 477
Quinn, J., Akerlof, C. W., Biller, S., et al. 1996, ApJL, 456, L83
Robertson, D. R. S., Gallo, L. C., Zoghbi, A., & Fabian, A. C. 2015, MNRAS, 453, 3455
Sahakyan, N., & Gasparyan, S. 2017, MNRAS, 470, 2861
Saito, S., Stawarz, Ł., Tanaka, Y. T., et al. 2013, ApJL, 766, L11
Sameer, K., Ganesh, N., Kumar, S., & Baliyan, K. S, V. 2015, ATel, 7495, 1
Scarpa, R., & Falomo, R. 1997, A&A, 325, 109
Shakura, N. I., & Sunyaev, R. A. 1973, A&A, 24, 337
Sikora, M., Begelman, M. C., & Rees, M. J. 1994, ApJ, 421, 153
Sokolov, A., & Marscher, A. P. 2005, ApJ, 629, 52
Stern, B. E., & Poutanen, J. 2014, ApJ, 794, 8
Striani, E., Verrecchia, F., Donnarumma, I., et al. 2010, ATel, 2686, 1
Suganuma, M., Yoshii, Y., Kobayashi, Y., et al. 2006, ApJ, 639, 46
Takahashi, T., Tashiro, M., Madejski, G., et al. 1996, ApJL, 470, L89
Tan, C., Xue, R., Du, L.-M., et al. 2020, ApJS, 248, 27
Tavecchio, F., Becerra-Gonzalez, J., Ghisellini, G., et al. 2011, A&A, 534, A86
Tavecchio, F., & Ghisellini, G. 2008, MNRAS, 386, 945
Urry, C. M., & Padovani, P. 1995, PASP, 107, 803
Villata, M., Raiteri, C. M., Balonek, T. J., et al. 2006, A&A, 453, 817
Wierzcholska, A., & Wagner, S. J. 2016, MNRAS, 458, 56
Wills, B. J., Wills, D., Breger, M., Antonucci, R. R. J., & Barvainis, R. 1992, ApJ, 398, 454
Xiao, H., Fan, J., Yang, J., et al. 2019, SCPMA, 62, 129811
Xiao, H. B., Pei, Z. Y., Xie, H. J., et al. 2015, Ap&SS, 359, 39
Xiao, H. B., Zhu, J. T., Fan, J. H., et al. 2022, MNRAS, 517, 4202
Xue, R., Liu, R.-Y., Petropoulou, M., et al. 2019, ApJ, 886, 23
Xue, R., Liu, R.-Y., Wang, Z.-R., Ding, N., & Wang, X.-Y. 2021, ApJ, 906, 51
Xue, R., Wang, Z.-R., & Li, W.-J. 2022, PhRvD, 106, 103021
Zabalza, V. 2015, ICRC, 34, 922
Zacharias, M., Sitarek, J., Dominis Prester, D., et al. 2017, ICRC, 301, 655
Zhang, J., Zhang, S.-N., & Liang, E.-W. 2013, ApJ, 767, 8
Zheng, Y. G., & Kang, T. 2013, ApJ, 764, 113